BBA - Biomembranes 1864 (2022) 183909

Contents lists available at ScienceDirect

BBA - Biomembranes

journal homepage: www.elsevier.com/locate/bbamem

Clustering of tetrameric influenza M2 peptides in lipid bilayers investigated by ^{19}F solid-state NMR

Madeleine Sutherland, Nhi Tran, Mei Hong *

Department of Chemistry, Massachusetts Institute of Technology, Cambridge, MA 02139, United States of America

ARTICLE INFO

Keywords:
Influenza M2
Clustering
^{19}F NMR
Spin diffusion
Depth of insertion

ABSTRACT

The influenza M2 protein forms a drug-targeted tetrameric proton channel to mediate virus uncoating, and carries out membrane scission to enable virus release. While the proton channel function of M2 has been extensively studied, the mechanism by which M2 catalyzes membrane scission is still not well understood. Previous fluorescence and electron microscopy studies indicated that M2 tetramers concentrate at the neck of the budding virus in the host plasma membrane. However, molecular evidence for this clustering is scarce. Here, we use ^{19}F solid-state NMR to investigate M2 clustering in phospholipid bilayers. By mixing equimolar amounts of 4F-Phe47 labeled M2 peptide and CF_3-Phe47 labeled M2 peptide and measuring F-CF_3 cross peaks in 2D ^{19}F—^{19}F correlation spectra, we show that M2 tetramers form nanometer-scale clusters in lipid bilayers. This clustering is stronger in cholesterol-containing membranes and phosphatidylethanolamine (PE) membranes than in cholesterol-free phosphatidylcholine and phosphatidylglycerol membranes. The observed correlation peaks indicate that Phe47 sidechains from different tetramers are less than ~2 nm apart. ^{1}H—^{19}F correlation peaks between lipid chain protons and fluorinated Phe47 indicate that Phe47 is more deeply inserted into the lipid bilayer in the presence of cholesterol than in its absence, suggesting that Phe47 preferentially interacts with cholesterol. Static ^{31}P NMR spectra indicate that M2 induces negative Gaussian curvature in the PE membrane. These results suggest that M2 tetramers cluster at cholesterol- and PE-rich regions of cell membranes to cause membrane curvature, which in turn can facilitate membrane scission in the last step of virus budding and release.

1. Introduction

Influenza A and B infections are responsible for an average of 35,000 deaths per year in the U.S. in recent years [1]. The 97-residue M2 protein of the influenza A virus plays several important roles in the virus life cycle. After the influenza virus enters a cell by endocytosis, the acidic environment of the endosome activates the tetrameric proton channel, acidifying the virion, which triggers fusion of the virus lipid envelope and the endosomal membrane and subsequent release of the viral ribonucleoproteins into the host cell [2–4]. The mechanism of proton conduction by M2 has been extensively characterized [5–12], and the mechanism of channel inhibition by adamantane drugs has also been elucidated using many biophysical methods [13–18]. In addition to the proton channel function, M2 mediates influenza virus budding and release by carrying out membrane scission independent of the host ESCRT machinery [19–21]. M2-deletion viruses can form buds on the plasma membrane but cannot be released, demonstrating this scission function [19].

Several lines of evidence suggest that M2 and other membrane proteins might cluster to carry out their functions. Electron micrographs of immunogold labeled M2 on the ~100 nm scale show that the protein is concentrated at the neck of the budding virions in influenza-infected MDCK cells [19]. Fluorescence microscopy images of rhodamine-labeled M2 on the 10 μm scale show that M2 preferentially localizes at the boundary of liquid-ordered (L_o) and liquid-disordered (L_d) phases in phase-separated giant unilamellar vesicles [19]. Functionally important cluster formation has also been reported for other membrane proteins. For example, fluorescence microscopy data revealed Gag-restricted clustering of the HIV Env protein upon virus maturation [22]. Co-clustering of the SNARE component syntaxin-1A and the pore-forming subunit of the Ca^{2+} channel Cav1.2 was associated with the interactions between these proteins in exocytotic neurotransmitter release [23].

Although biophysical data have shown that M2 co-localizes on the micron and ~100 nm scale, whether these tetramers associate on the molecular length scale of a few nanometers has not been established

* Corresponding author.
E-mail address: meihong@mit.edu (M. Hong).

https://doi.org/10.1016/j.bbamem.2022.183909
Received 30 October 2021; Received in revised form 8 February 2022; Accepted 5 March 2022
Available online 8 March 2022

experimentally. Coarse-grained molecular dynamics simulations found that M2 tetramers spontaneously assemble into compact clusters or linear aggregates in response to entropic driving forces, and these clusters occur at the neck of the budding virus where membrane lateral stress is high [24]. Deuterium NMR spectra of M2(22–46) peptides containing deuterated Ala_{29} in DOPC: DOPE (4:1) bilayers showed that increasing the peptide/lipid molar ratio increased the quadrupolar couplings. Simulations of these ^{2}H NMR lineshapes indicate that the uniaxial rotational diffusion rates of the tetramers slowed by 25-fold [25], suggesting protein clustering. However, since protein diffusion rates also decrease with increasing membrane viscosity as more protein is added to the membrane, this dynamics change does not provide unambiguous evidence of clustering of the tetramers.

Cholesterol binding to M2 might provide a molecular mechanism for M2 clustering [26–29]. The virus budding sites or "budozones" to which M2 is partitioned to contain higher concentrations of cholesterol than the rest of the plasma membrane [19,24], and the L_o phase is also rich in cholesterol compared to the L_d phase [19]. Recent solid-state NMR experiments that measure ^{13}C—^{19}F distances between ^{13}C-labeled M2 (22–61) and fluorinated cholesterol showed that the methyl-rich β-face of cholesterol interacts with the methyl-rich Ile and Leu residues in the M2 transmembrane (TM) helix. Meanwhile, the polar hydroxyl group of cholesterol interacts with the polar and aromatic residues in the amphipathic helix (AH) [28]. These ^{13}C—^{19}F distance data further showed that on average, two cholesterol molecules are bound to each M2 tetramer, forming an asymmetric protein-cholesterol complex. It was hypothesized that this sub-stoichiometric complex might facilitate the recruitment of M2 tetramers to the virus budozone because of the higher cholesterol concentration in the budozone compared to the plasma membrane. More recent ^{19}F and ^{13}C spin diffusion NMR data revealed that cholesterol molecules exist as dimers and tetramers in lipid bilayers, with the smooth α-face preferentially interacting with each other [30]. This means that the rough β-face could interact with proteins, suggesting that cholesterol dimers might act as the "glue" that clusters multiple M2 tetramers.

Here we employ ^{19}F magic-angle-spinning (MAS) NMR spectroscopy to investigate whether M2 tetramers form nanoscale clusters in lipid bilayers, and we characterize the lipid composition and amino acid sequence requirements for clustering. We synthesize a 40-residue M2 peptide (residues 22–61) that contains both the transmembrane (TM) and amphipathic helix (AH) domains. We also synthesize a 28-residue M2 peptide (residues 22–49) that contains the TM domain and the $^{47}FFK^{49}$ hinge. We incorporate either 4F-labeled Phe47 or 4-CF_3-labeled Phe47 into these peptides. Using equimolar mixtures of the 4F-Phe47 labeled and CF3-Phe47 labeled peptides in lipid membranes, we conduct 2D ^{19}F—^{19}F spin diffusion correlation NMR experiments to measure the spatial proximity of the differently labeled peptides. ^{19}F NMR provides a unique opportunity for probing nanometer-scale spatial proximity of membrane proteins. The lack of ^{19}F background in proteins allows us to incorporate and detect sparsely fluorinated residues [31,32]. ^{19}F has large isotropic and anisotropic chemical shifts, such that it is sensitive to molecular conformation and dynamics. Most importantly, ^{19}F has a large gyromagnetic ratio (γ), which increases its dipolar coupling strengths compared to low-γ nuclei. Thus, ^{19}F NMR is well suited for measuring long interatomic distances [33–36]. Recently, ^{19}F spin diffusion NMR experiments have been shown to be able to detect inter-fluorine distances of up to ~2 nm [37–40]. Spin diffusion between a CF_3 and a CF group is even more efficient than CF-CF spin diffusion, because of the simultaneous polarization transfer of three fluorines to a CF group. Using this ^{19}F spin diffusion NMR approach, we demonstrate that M2 tetramers indeed form clusters in lipid membranes, and this clustering is facilitated by cholesterol and PE lipids. We also probe the depth of insertion of Phe47 at the junction of the TM and AH using ^{1}H—^{19}F 2D correlation NMR experiments [41], and relate these observations to M2 clustering.

2. Materials and methods

2.1. Peptide synthesis and purification

All M2 peptides in this study were synthesized using Fmoc solid-phase chemistry on a custom designed flow peptide synthesizer [42]. Two peptides were synthesized. M2CD (residues 22–61) contains both the TM helix and the amphipathic helix and has the amino acid sequence H-^{22}SSDPLVVAA SIIGILHLIL WILDRLFFKS IYRRLKYGLK R^{61}-NH_2. The segment ^{53}RRLKY^{57} in the amphipathic helix corresponds to the Weybridge strain [28], while the commonly studied Udorn strain of M2 has ^{53}RFFEH^{57} at the corresponding positions. Both sequences interact with cholesterol [28]. M2TM (residues 22–49) has the amino acid sequence H-^{22}SSDPLVVAA SIIGILHLIL WILDRLFFK^{49}-NH_2. This peptide is three residues (^{47}FFK^{49}) longer than the commonly studied TM peptide (residues 22–46). Each peptide contained either a 4-CF_3-Phe47 label or a 4F-Phe47 label. In addition, M2CD also contained ^{13}C, ^{15}N-labeled G34 and I51 and CD_3-labeled A29, while M2TM also contained ^{13}C, ^{15}N-labeled V27, A30 and G34 (Table 1). These ^{13}C, ^{15}N labeled residues allow us to verify the secondary structure of these peptides in the lipid membranes.

Each M2 peptide was synthesized on the 0.05 mmol scale using H-Rink amide ChemMatrix resin (0.1 g at 0.05 mmol/g loading size). The resin was swelled in the reaction vessel for 5 min in ~5 mL of *N*,*N*-dimethylformamide (DMF) at 70 °C. A 10-fold excess (0.5 mmol) of unlabeled amino acid was singly coupled with a coupling time of 40 s, using hexafluorophosphate azabenzotriazole tetramethyl uronium (HATU) as the coupling agent. After the final coupling step, the peptide was deprotected and cleaved from the resin by addition of trifluoroacetic acid (TFA)/phenol/water/triisopropyl silane solution (88:5:5:2 by volume) in a fritted syringe, under vortex agitation, at room temperature for 3 h. The resin was filtered off, and the crude peptide was precipitated and triturated three times with ~11 mL cold diethyl ether. The remaining solvent was allowed to evaporate from the crude peptide in the fume hood overnight.

To purify M2CD, we dissolved crude peptide in 30% acetonitrile and conducted reverse-phase HPLC using a Vydac C4 column (22 mm × 250 mm, 10 μm particle size). All HPLC procedures were run in the presence of 0.1% TFA. A linear gradient of 30–70% acetonitrile was applied over 44 min at a flow rate of 15 mL/min. The peptide eluted at 64% acetonitrile. The collected HPLC fractions were dried under nitrogen to remove most of the acetonitrile, then lyophilized overnight to obtain a homogeneous powder. MALDI mass spectrometry data verified the mass

Table 1
Isotopic labeling and membrane compositions of the influenza AM2 samples used in this study. 4-CF_3 or 4-F-labeled Phe47 residues are underlined and shown in red. ^{13}C, ^{15}N-labeled residues are bolded and shown in blue. CD_3-labeled Ala is italicized.

M2CD(22-61)

```
22  25    30    35    40    45    50    55    60
SSD PLVVA ASIIG ILHLI LWILD RLFFK SIYRR LKYGL KR
```

Membrane Samples	P : L : C molar ratio	Lipid composition
1	1 : 12 : 3 : 3	POPC : POPG : chol
2	1 : 12 : 3	POPC : POPG
3	1 : 24 : 6 : 6	POPC : POPG : chol
4	1 : 24 : 6	POPC : POPG
5	1 : 30	POPE

M2TM(22-49)

```
22  25    30    35    40    45
SSD PLVVA ASIIG ILHLI LWILD RLFFK
```

Membrane Samples	P : L : C molar ratio	Lipid composition
6	1 : 24 : 6 : 6	POPC : POPG : chol
7	1 : 24 : 6	POPC : POPG

of CF_3-Phe47 labeled M2CD to be 4766.8 Da, in good agreement with the calculated mass of 4764.8 Da. For 4F-Phe47 labeled M2CD, the measured mass was 4715.2 Da, in good agreement with the calculated mass of 4713.8 Da.

4F-Phe47 labeled M2TM peptide was purified by HPLC using a linear gradient of 30–100% acetonitrile in water over 65 min at a flow rate of 10 mL/min. The peptide eluted at 81% acetonitrile. MALDI-MS analysis verified the mass to be 3180.1 Da, in excellent agreement with the calculated mass of 3179.9 Da. HPLC fractions were dried under nitrogen gas and lyophilized overnight to obtain a powder. The total synthesis and purification yield was 5%. For CF_3-Phe47 labeled M2TM, crude peptide was dissolved in 60% acetonitrile, and purified by reverse-phase HPLC using a linear gradient of 80–99% acetonitrile in water over 54 min at a flow rate of 10 mL/min. The peptide eluted at 83% acetonitrile. MALDI-MS analysis verified the mass to be 3228.3 Da, in good agreement with the calculated mass of 3229.9 Da. The total yield was 10%. For all peptides, only HPLC fractions with purities higher than 90% were used.

2.2. Preparation of proteoliposomes

We used three phospholipids in this study: 1-palmitoyl-2-oleoyl-sn-glycero-3-phosphocholine (POPC), 1-palmitoyl-2-oleoyl-sn-glycero-3-phospho-(1′-rac-glycerol) (POPG), and 1-palmitoyl-2-oleoyl-sn-glycero-3-phosphoethanolamine (POPE). All lipids and cholesterol were purchased from Avanti Polar Lipids and used without further purification. The POPX (X = C, G, E) lipids were chosen to mimic the acyl chain compositions of biological membranes. These lipids were mixed with cholesterol (chol) to produce three membranes: POPC: POPG (4:1), POPC: POPG: chol (4:1:1, i.e. 17 mol% cholesterol), and POPE. The NMR samples contained 4.5–8.0 mg of peptide and 12–48 mg of lipids and cholesterol. The peptide/lipid molar ratios (P/L) refer to the ratio of M2 monomers to all phospholipids, excluding cholesterol. P/L values of 1:15 and 1:30 were used in this study. These 1:30 and 1:15 samples are more dilute compared to the samples in the recent ^{2}H NMR study, which had a P/L ratio of 1:7.5 [25].

We began the sample preparation by dissolving the appropriate mass of M2 peptide in 500 μL trifluoroethanol (TFE) and dissolving phospholipids and cholesterol in 200–500 μL chloroform. One Pasteur pipet drop of methanol was added to POPE to aid dissolution. The homogeneous lipid solution was added to the peptide TFE solution and incubated at room temperature for at least 10 min, then the organic solvent was removed using nitrogen gas. The dried peptide-lipid film was resuspended in 2 mL buffer (10 mM pH 7.4 HEPES/NaOH buffer, 1 mM EDTA, and 0.1 mM NaN_3) and homogenized by one of two methods. The POPC: POPG membranes with or without cholesterol were subjected to 10–15 cycles of freeze-thawing between liquid nitrogen and a warm (37–50 °C) water bath. The POPE vesicle suspension, which does not homogenize well by freeze-thawing, was sonicated at room temperature using a bath sonicator for at least three rounds of seven minutes each until the suspension appeared homogeneous. All proteoliposome suspensions were transferred to Thermo Scientific Snakeskin™ dialysis tubing with a 3.5 kD MWCO and dialyzed three times for 8–12 h each in sample buffer to remove residual TFE. TFE removal was important for preventing its ^{19}F NMR signal from interfering with the measurement of the peptide ^{19}F—^{19}F cross peaks. The success of the TFE/TFA removal was confirmed by the absence of a ^{19}F signal at −78 ppm in the 1D ^{19}F direct polarization (DP) spectra. The proteoliposome suspensions were ultracentrifuged to obtain the membrane pellets. Some samples were spun down using a Beckman Coulter Optima LE-80 K centrifuge equipped with a SW-60 swinging bucket rotor at 40,000–45,000 rpm (143,000–272,000 ×g) at 4 °C for 4–5 h. Other samples were spun down at 55,000 rpm (max 186,000 ×g) in a Beckman Coulter Optima Max preparative ultracentrifuge equipped with a TLA-55 rotor for two hours. The wet membrane pellets were allowed to dry in a desiccator or under nitrogen gas until the water content is 40–50 wt% of the total pellet mass. The hydration level was measured gravimetrically. When the volume of excess water was large, brief lyophilization was used to remove some of the bulk water prior to nitrogen drying. The samples were spun into a 4 mm MAS rotor using a 5 mL pipette tip in a Thermo Sorvall ST 16R centrifuge.

2.3. Solid-state NMR experiments

MAS NMR experiments were conducted on a Bruker 400 MHz (^{1}H Larmor frequency) wide-bore AVANCE III-HD spectrometer using a 4 mm Bruker HFX MAS probe tuned to ^{1}H, ^{19}F and ^{13}C Larmor frequencies. ^{31}P chemical shifts were referenced to the hydroxyapatite signal at 2.73 ppm on the phosphoric acid scale. ^{19}F chemical shifts were referenced to the Teflon signal at −122 ppm. ^{1}H chemical shifts were referenced to the POPC headgroup Hγ signal at 3.26 ppm on the TMS scale, or to the lipid chain-end methyl ^{1}H signal at 0.9 ppm in POPE samples, since POPE has no headgroup γ protons. ^{13}C chemical shifts were calibrated using the ^{13}Cα signal of glycine at 43.65 ppm on the TMS scale. Typical radio-frequency (RF) field strengths were 50–63 kHz for ^{19}F, 50–71 kHz for ^{1}H, and 50 kHz for ^{13}C. 1D ^{13}C and 2D ^{13}C—^{13}C correlation experiments used a ^{1}H excitation pulse RF field strength of 71 kHz. Static ^{31}P NMR spectra were measured using a Bruker 4 mm ^{1}H/^{31}P probe at 298 K and 310 K. The ^{31}P RF field strength was 62.5 kHz, and 1024 scans were measured per spectrum.

The 2D ^{19}F—^{19}F correlation spectra were measured using a CORD (Combined $R2_n^\nu$-driven) [43] spin diffusion mixing time of 500 ms. Cross peak intensities between 4-CF_3-Phe47 and 4F-Phe47 report the spatial proximity between the two fluorines. The 2D ^{19}F correlation experiment begins with ^{1}H—^{19}F cross polarization (CP), followed by ^{19}F chemical shift evolution under ^{1}H TPPM decoupling [44] and the CORD mixing period before detection. The unsynchronized 2D ^{19}F—^{19}F correlation spectra were measured under 8.5 kHz MAS. The indirect dimension spectral width was 211 ppm, and the maximum t_1 evolution time was 0.567 ms. For each sample, four to eight blocks of 2D spectra were coadded to obtain sufficient signal-to-noise ratios (SNRs) and to correct for field drift between blocks. The total measuring time was 70–123 h for each sample (Table 2). To increase the spectral sensitivity, we also measured rotor synchronized 2D ^{19}F spectra that remove the spinning sidebands in the indirect dimension. For these experiments, the indirect dimension spectral width was set to 23 ppm and the MAS frequency was 8641 Hz, so that the t_1 increment was one rotor period, or 115.73 μs. A total of 28 complex t_1 time points were collected to give a maximum evolution time of 1.62 ms. With the small spectral width in the indirect dimension, the 4F-Phe47 peak was folded to −71 ppm. Four to eight blocks of 2D spectra were coadded for each sample to obtain sufficient SNRs, giving a total measuring time of 88–105 h per sample (Table 2).

To reduce peptide motion and ensure that the measured ^{19}F—^{19}F cross peaks reflect intermolecular proximities, these 2D ^{19}F—^{19}F correlation experiments were conducted at ~243 K (−30 °C) using an FTS unit, which cooled house air to −85 to −78 °C and outputted it to the MAS probe at a flow rate of 1700–1850 L/h. All reported temperatures are direct thermocouple readings, and are ~5 °C lower than the actual sample temperature estimated based on the water ^{1}H chemical shifts [45].

To investigate the depth of insertion of Phe47 in the lipid membrane, we measured 2D ^{1}H—^{19}F heteronuclear correlation (HETCOR) spectra with ^{1}H spin diffusion [41]. The experiment begins with four ^{19}F 90° pulses spaced by 2 ms each to saturate the ^{19}F magnetization. Then a ^{1}H 90° excitation pulse and a ^{1}H T_2 filter of 2*112.6 μs = 225.2 μs are used to select the water and lipid ^{1}H magnetization. The ensuing ^{1}H chemical shift evolution is followed by a ^{1}H mixing time of 100 ms during which the water and lipid ^{1}H magnetization is transferred to the peptide and is detected on ^{19}F after ^{1}H—^{19}F CP. These 2D HETCOR experiments used 48 t_1 time points to reach a maximum ^{1}H t_1 evolution time of 4.8 ms, and 1024 scans per t_1 slice. Typical spectra were coadded from four blocks of

Table 2
Parameters for the 2D ^{19}F—^{19}F and ^{1}H—^{19}F NMR experiments.

Experiment	NMR parameters	Experimental time (hrs)	Membrane sample
rotor synchronized 2D FF CORD	B_0 = 9.4 T, T_{set} = 243–245 K, ν_r = 8641 Hz, SWH1 = 8641 Hz (=23 ppm), SWH2 = 93.75 kHz, ^{19}F carrier frequency = −68 ppm, NS per block =1024, τ_{rd} = 1.7 s, $t_{1,max}$ = 1.62 ms, $t_{1,inc}$ = 115.8 μs, τ_{dwell} = 5.3 μs, τ_{acq} = 4.3 ms, $\tau_{HF=}$1 ms, τ_{CORD} = 500 ms, $\nu_{1H,acq}$ = 71.4 kHz (samples 3,4, and 6) and 62.5 kHz (samples 5 and 7).	105 105 105 87.5 87.5	3 4 5 6 7
2D FF CORD without rotor synchronization	B_0 = 9.4 T, T_{set} = 243 K, ν_r = 8500 Hz, SWH1 = 79.4 kHz, SWH2 = 93.75 kHz, ^{19}F carrier frequency = −90.2 ppm, NS per block = 256, τ_{rd} = 2 s, $t_{1,max}$ = 0.567 ms, $t_{1,inc}$ = 12.60 μs, τ_{dwell} = 5.3 μs, τ_{acq} = 4.27 ms, τ_{HF} = 1 ms, τ_{CORD} = 500 ms, $\nu_{1H,acq}$ = 71.4 kHz.	122.5 105 140 70	1 2 3 4
2D ^{1}H—^{19}F HETCOR with 100 ms ^{1}H spin diffusion	B_0 = 9.4 T, T_{set} = 262–265 K for samples 3, 4, 6, 7 and 283 K for sample 5, SWH1 = 5 kHz, SWH2 = 93.75 kHz, ^{19}F carrier frequency = −97.6 ppm, NS per block = 1024, τ_{rd} = 1.5 s, $t_{1,max}$ = 4.8 ms, $t_{1,inc}$ = 200 μs, τ_{dwell} = 5.3 μs, τ_{acq} = 4.3 ms, τ_{HF} = 1 ms, T_2-filter duration = 117.6 μs, τ_{mix} = 100 ms, $\nu_{1H,acq}$ = 71.4 kHz for sample 3 and 50 kHz for samples 4–7.	88 88 88 88 88	3 4 5 6 7

Symbols: B_0 = magnetic field; T_{set} = thermocouple-reported bearing gas temperature; ν_r = MAS frequency; SWH1: spectral width of the ω_1 dimension of the 2D spectra; SWH2: spectral width of the ω_2 dimension of the 2D spectra; ns = number of scans per t_1 slice of the 2D spectra; τ_{rd} = recycle delay; $t_{1,max}$ = maximum t_1 evolution time; $t_{1,inc}$ = increment or dwell time for the t_1 evolution period; τ_{dwell} = dwell time during direct acquisition of the FID; τ_{acq} = maximum acquisition time during direct detection; τ_{HF} = ^{1}H–^{19}F CP contact time; τ_{CORD} = CORD mixing time. $\nu_{1H,\ acq}$ = ^{1}H decoupling field strength during detection.

experiments, giving signal-averaging times of 88 h per sample. For different lipid membranes, we chose sample temperatures of 262 to 283 K (−11 to +12 °C; Fig. 6) to obtain similar lipid CH_2 linewidth of about 350 Hz, as assessed from 1D ^{1}H MAS spectra. This ensures that the lipid chain dynamics are similar between the different membranes, thus giving similar ^{1}H spin diffusion coefficients. All NMR spectra were plotted from TopSpin 3.6.1. Peak intensities were analyzed in Microsoft Excel v16.52.

3. Results

In this study, we investigate M2 clustering in lipid membranes as a function of the peptide/lipid ratio, the presence or absence of cholesterol, and the lipid composition of the membrane. We also compare M2 peptides that contain both the TM domain and the amphipathic helix (M2CD) versus only the TM domain and the hinge (M2TM). The POPC: POPG (4:1) membrane composition and the peptide lengths were chosen to allow comparison of our data with previous biochemical studies of the membrane scission function of M2 [19,46–48] and with NMR [27,28] and EPR [49–51] studies of M2 interaction with cholesterol.

Our strategy for detecting M2 tetramer association is to mix 4-CF_3-Phe47 labeled peptide with 4F-Phe47 labeled peptide at a 1:1 molar ratio and measure CF_3-F cross peaks in 2D ^{19}F—^{19}F correlation spectra. Phe47 is chosen because it lies at the four corners of the tetramer in both M2CD and M2TM, with maximal separation between monomers within each tetramer, and potentially the shortest distance between two tetramers (Fig. 1). Based on the eight lowest energy structures of M2CD (residues 22–62) in DOPC: DOPE bilayers (PDB: 2L0J) [52] solved at 30 °C, the distances between the *para* hydrogen positions of the nearest-neighbor Phe47 sidechains within each tetramer range from 21 Å to 33 Å. The average distance, 28 Å, is too long to be measured by ^{19}F spin diffusion NMR, whose detection upper limit is ~20 Å [38]. For M2TM, a solution NMR structure of M2(19–49) in DPC micelles [53] indicates a distance of ~23 Å between the *para* hydrogens of F47 on different chains (PDB 2MUV), again indicating that intra-tetramer Phe47-Phe47 distances are too long to be measurable. Thus, the hinge residue of Phe47 is a good candidate for probing the presence or absence of tetramer clustering for both M2CD and M2TM.

We next estimate the closest approach between M2 tetramers if the tetramers are uniformly distributed in the membrane. Molecular dynamics simulations of gel-phase POPC membranes indicate a headgroup area per lipid of 59 $Å^2$ [54]. For POPG the area/lipid is 60.6 $Å^2$ based on scattering density profiles [55,56]. If we assume that all M2 tetramers are parallel aligned, which would give rise to the shortest approach between Phe47 residues of two adjacent tetramers, then at a P/L ratio of 1:30, the center-to-center distance between two nearest-neighbor tetramers is about 66 Å. When P/L increases to 1:15, the center-to-center distance decreases to 51 Å. Since each M2CD tetramer has a side length of around 28 Å, these values correspond to closest-approach distances of ~38 Å (P/L 1:30) and ~ 23 Å (P/L 1:15) between the *para* hydrogens of Phe47 of two different tetramers. These inter-tetramer separations for homogeneously distributed M2 are beyond the detection limit of ^{19}F spin diffusion NMR. If M2 tetramers are randomly aligned, with both antiparallel and parallel orientations possible, then the closest-approach distance between two tetramers will be even longer and hence undetectable for this homogeneous distribution model. However, if the tetramers cluster together in the membrane, then CF_3-F cross peaks can become observable. We test this hypothesis

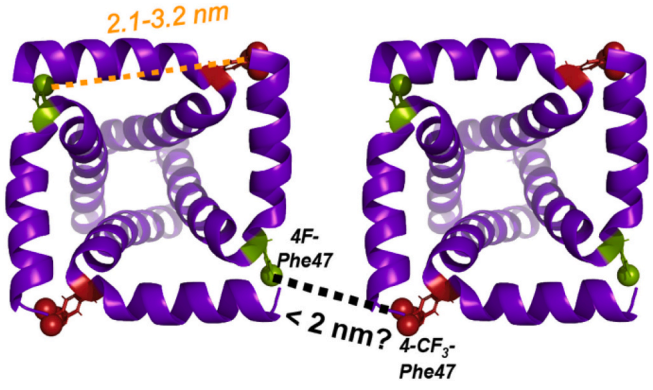

Fig. 1. Schematic diagram of M2 clustering in lipid membranes. Two copies of the solid-state NMR orientational structure of M2(22–62) (PDB: 2L0J), manually positioned to illustrate how two 4F-Phe47 and CF_3-Phe47 residues on two neighboring tetramers might approach each other within ~2 nm. This close approach is required to explain the observation of ^{19}F—^{19}F cross peaks in 2D ^{19}F spin diffusion spectra. Intra-tetramer nearest-neighbor distances between Phe47 sidechain *para*-hydrogens are 2.1–3.3 nm.

by measuring 2D ^{19}F—^{19}F correlation spectra as a function of P/L and membrane compositions.

3.1. M2 tetramers cluster in a membrane-dependent manner

We first measured the ^{13}C chemical shifts of site-specifically labeled M2CD and M2TM peptides to verify that Phe47 fluorination does not perturb the α-helical conformation of the peptide (Fig. 2). The ^{13}C chemical shifts of G34 and I51 in M2CD and V27, A30 and G34 in M2TM all correspond to the α-helical conformation in both POPC: POPG membranes and the POPE membrane, confirming that the helical conformation of the TM and AH domains is preserved. This α-helicity is consistent with previously reported chemical shifts of M2 peptides in a variety of lipid membranes [16,28,57,58] and with the periodicity of orientation-dependent ^{15}N—^{1}H dipolar couplings of M2CD in PC and PE membranes [52]. The ^{19}F CP spectra of the peptides show the expected CF_3-Phe and 4F-Phe peaks at −61 ppm and − 116 ppm, respectively. CF_3 spinning sidebands are also observed, but there is no detectable signal from TFE or TFA, indicating successful removal of the fluorinated solvents. The 4F-Phe peak is broader and lower in intensity than the CF_3 peak: the linewidths are 4.0–5.5 ppm for 4F-Phe and 3.0–3.7 ppm for CF_3 under these experimental conditions. These differences are expected because the *para*-fluorine group is more sensitive to sidechain conformational disorder than the fast-rotating methyl group. The CF_3 spinning sideband intensity of M2CD is higher in the POPE membrane than in the POPC: POPG membranes, suggesting that the Phe47 sidechain is more immobilized in the POPE membrane.

Fig. 3 shows the 500 ms 2D ^{19}F—^{19}F CORD spectra of M2CD in POPC: POPG membranes with and without cholesterol. At a high P/L of 1:15, we observed a clear F-CF_3 cross peak in the POPC: POPG: chol membrane but a weaker cross peak in the POPC: POPG membrane (Fig. 3a, c). When the peptide concentration was decreased two-fold to P/L 1:30 (Fig. 3b, d), the F-CF_3 cross peak persisted in the POPC: POPG: chol membrane. Moreover, its intensity is similar between the low and high peptide concentrations (Fig. 3e, *top*), suggesting that M2 tetramers cluster rather than distributing homogeneously in the cholesterol-containing membrane. In contrast, dilution of the peptide in the POPC: POPG membrane completely suppressed the F-CF_3 cross peak, indicating that the intra-tetramer Phe47-Phe47 distances are too long to be measurable. If the 2D experiment were mainly detecting intra-tetramer cross peaks, it would be difficult to explain the dependence of these cross peak intensities on the membrane composition and peptide concentration. Therefore, these results indicate that M2 tetramers cluster in the cholesterol-containing membrane, and this clustering is not an artifact of the high peptide concentration but reflects specific protein-protein, and possibly protein-cholesterol, interactions.

To reproduce the F-CF_3 cross peaks with higher sensitivity, we measured rotor-synchronized 2D ^{19}F correlation spectra of the 1:30 M2CD samples, and quantified the intensity of the F-CF_3 cross-peak relative to the summed intensities in the −71 ppm cross section of the 4F-Phe47 peak (Fig. 4). The cross-peak intensities varied significantly between different membrane samples. In the POPC: POPG: chol sample, the F-CF_3 cross peak intensity is 14 ± 3% of the total 4F-Phe47 intensity (Fig. 4a), whereas in the POPC: POPG membrane, the cross peak relative intensity decreased to 6 ± 3% of the total intensity (Fig. 4b), confirming that cholesterol facilitates clustering. To investigate whether M2 can also cluster in other membranes, we measured the 2D ^{19}F—^{19}F correlation spectrum of M2CD bound to the POPE membrane. PE lipids are enriched in influenza virus lipid envelopes relative to the host cell membranes from which they are derived [59,60], and their negative curvature is known to play an important role in membrane fusion and fission in general [61,62]. Fig. 4c shows the 2D ^{19}F spin diffusion spectrum of POPE-bound M2CD. A strong CF_3-F cross peak is observed, whose relative intensity, 26 ± 3%, is even higher than that of the POPC: POPG: chol sample, indicating that M2CD clusters more strongly in the POPE membrane.

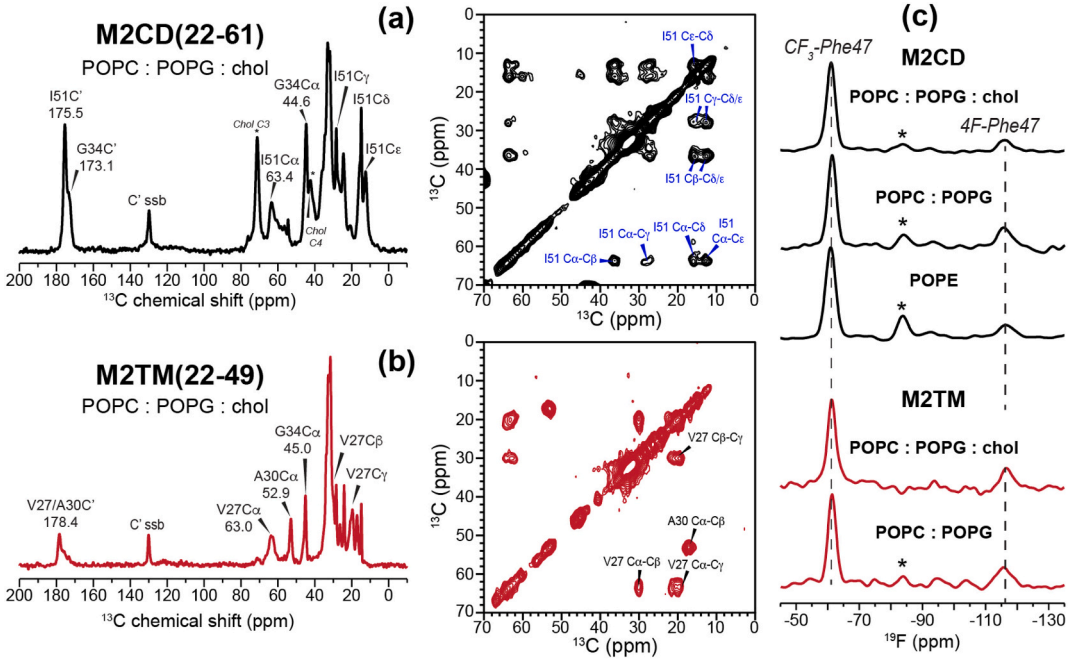

Fig. 2. ^{13}C and ^{19}F NMR spectra of membrane-bound M2 peptides. (a) 1D ^{13}C CP and 2D ^{13}C—^{13}C correlation spectra of M2CD at P/L 1:15 in POPC: POPG: chol membranes. The spectra were measured at 243 K under 10 kHz MAS. Peaks that are not annotated in the 1D spectra are lipid ^{13}C signals. The sample contains C3, C4-labeled cholesterol (peaks marked with * in the M2CD 1D spectrum). (b) 1D and 2D ^{13}C spectra of M2TM at P/L 1:30 in POPC: POPG: chol membranes. The spectra were measured at 253 K under 9 kHz MAS. The peptide ^{13}C chemical shifts confirm the α-helical conformation of M2CD and M2TM. (**c**) ^{19}F CP spectra of membrane-bound M2CD and M2TM. Similar ^{19}F linewidths and intensity distributions are observed for both M2CD and M2TM, indicating that the two peptides exhibit similar conformational dynamics under these experimental conditions. The spectra in (c) were measured between 262 K and 283 K under 8.5 kHz MAS. Asterisks indicate the spinning sideband of the CF_3 peak.

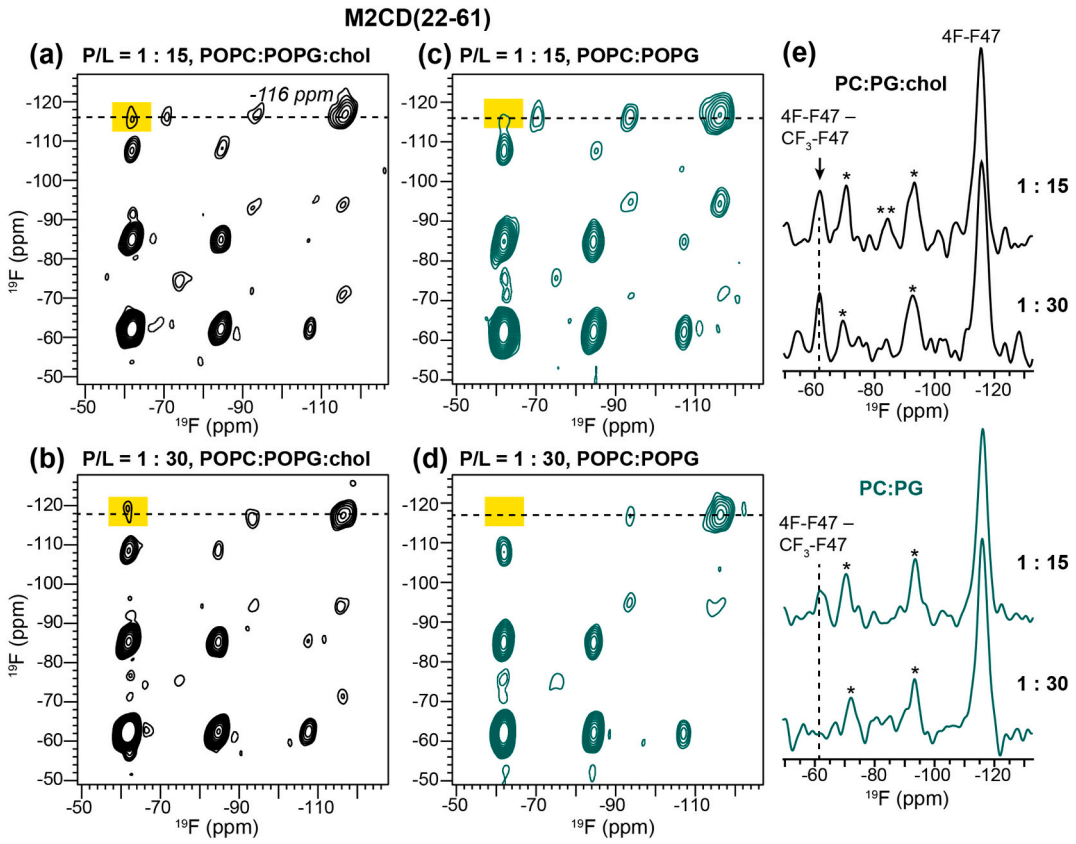

Fig. 3. 500 ms 2D $^{19}F—^{19}F$ CORD spectra of mixed Phe47-fluorinated M2CD in lipid membranes. The spectra were measured at 243 K under 8.5 kHz MAS. The −116 ppm cross sections of 4F-Phe47 are shown on the right. The presence of a cross peak between 4F-Phe47 and 4-CF_3-Phe47 (−62 ppm) indicates an inter-tetramer contact. F-CF_3 cross peaks are observed at high P/L in both membranes, but only in the cholesterol-containing membrane at the low P/L of 1:30. (a) 2D spectrum of M2CD in POPC: POPG: chol membranes, at P/L 1:15. (b) 2D spectrum of M2CD in POPC: POPG: chol membranes at P/L 1:30. (**c**) 2D spectrum of M2CD in POPC: POPG membranes, at P/L 1:15. (d) 2D spectrum of M2CD in POPC: POPG membranes at P/L 1:30. (e) Cross sections of the spectra in (a–d) at the 4F-Phe ω_1 chemical shift of −116 ppm (marked with dashed lines in the 2D spectra). Dashed lines guide the eye to the 4F – CF_3 cross peak. Single asterisks (*) denote spinning sidebands of the 4F-Phe47 peak while double asterisks (**) denote the CF_3 spinning sideband.

To determine whether the amphipathic helix is required for M2 clustering, we also measured the 2D ^{19}F spin diffusion spectra of M2TM (22–49) in POPC: POPG membranes with and without cholesterol. At P/L 1:30, we observed a clear F-CF_3 cross peak in the POPC: POPG: chol membrane but the cross peak is much weaker in the POPC: POPG membrane (Fig. 5). This trend is similar to M2CD, indicating that the TM peptide is able to cluster in the absence of the AH residues 50–62; moreover, this clustering is also facilitated by cholesterol. The F-CF_3 cross peak intensities of M2TM are stronger than that of M2CD (Fig. 5c), suggesting that M2TM peptides may form tighter clusters than M2CD.

3.2. Depth of insertion of Phe47 in lipid membranes

Using fluorinated Phe47, we next investigated the depth of insertion of the ^{47}FFK^{49} hinge between the TM and AH domains in different membranes. We used the 2D $^{1}H—^{19}F$ correlation experiment with ^{1}H spin diffusion for this purpose [41]. By detecting the cross peaks of the CF_3-Phe47 signal with the water ^{1}H signal at 4.8–5.1 ppm and with the lipid ^{1}H signal at 1.3 ppm, we obtain information about the depth of insertion of the TM-AH junction in different lipid membranes. The 4F-Phe47 signal at −116 ppm reports the same information, but due to its low intensity we do not analyze its signal. Fig. 6 compares the 100 ms 2D $^{1}H—^{19}F$ HETCOR spectra of the different membrane samples. All samples exhibit strong water-Phe47 cross peaks, as expected because of the surface-exposed position of this residue [50,52]. The depth of insertion of Phe47 is manifested by the lipid-CF_3 cross peak intensity relative to the water-CF_3 cross peak intensity, I_{CH2}/I_{H2O}. For M2CD, the intensity ratios are similar (0.16 and 0.13) between the POPC: POPG: chol membrane and POPC: POPG membranes (Fig. 6a, b). This indicates that the Phe47 sidechain is moderately inserted into both membranes. In dramatic contrast, the lipid-to-water intensity ratio is much higher, 0.74, for M2TM in the POPC: POPG: chol membrane (Fig. 6c), indicating that Phe47 in the TM peptide is in close contact with the lipid chains. Repeating this measurement for M2TM in the cholesterol-free POPC: POPG membrane decreased the lipid-CF_3 cross peak intensity to 0.13 (Fig. 6d). These spectra were measured at temperatures at which the lipid chains have similar ^{1}H linewidths. Thus, the high intensity of the lipid-Phe47 cross peak in the POPC: POPG: chol membrane cannot be attributed to different spin diffusion coefficients, but rather reflect deeper insertion of the Phe47 sidechain of the TM peptide in the cholesterol-containing membrane. Finally, we measured the 2D $^{1}H—^{19}F$ HETCOR spectrum of M2CD in the POPE membrane. In contrast to the POPC: POPG samples, the spectrum shows negligible lipid cross peak intensity (Fig. 6e), indicating that Phe47 is much more shallowly inserted into the POPE membrane than the POPC: POPG membranes.

3.3. M2CD induces curvature to POPE membranes

Membrane scission requires negative Gaussian curvature (NGC), wherein every point on the surface of the membrane has principal curvatures of opposite signs. This NGC is manifested as a broad isotropic peak in the static ^{31}P NMR spectra [63] and as diffraction peaks at characteristic Q positions in small-angle X-ray scattering (SAXS) data [64]. A previous SAXS study showed that M2CD and full-length M2

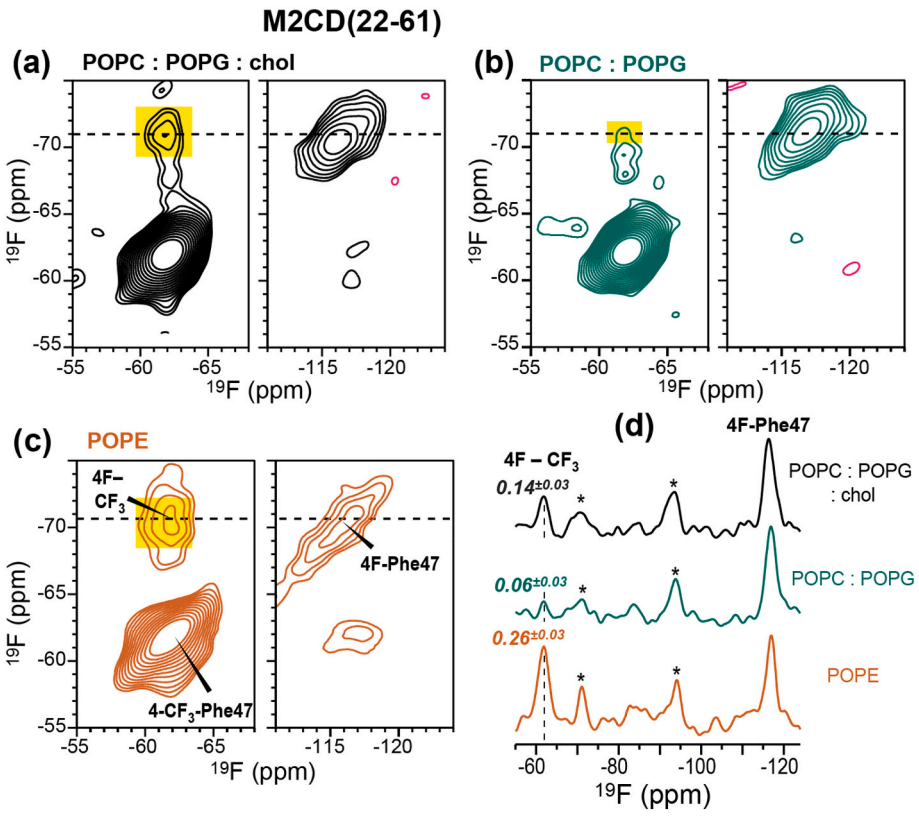

Fig. 4. 2D ^{19}F—^{19}F correlation spectra of mixed Phe47 fluorinated M2CD peptides in three membranes at P/L 1:30. The spectra were measured with 500 ms CORD mixing at 243 K under 8641 Hz MAS. (a) 2D spectrum of the peptide in the POPC: POPG: chol membrane. (b) 2D spectrum of the peptide in the POPC: POPG membrane. (c) 2D spectrum of the peptide in the POPE membrane. (d) 1D cross sections at the folded 4F-Phe47 chemical shift of −71 ppm. The CF_3 cross peak (dashed line) intensity relative to the sum of all peak intensities in the cross section decreases in the order of POPE > POPC: POPG: chol > POPC: POPG. Asterisks (*) denote spinning sidebands of the 4F-Phe47 signal.

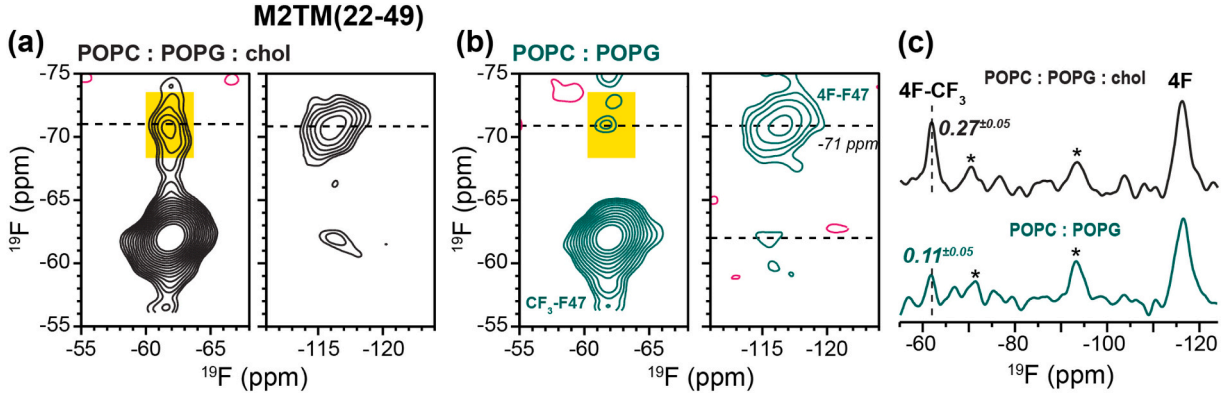

Fig. 5. 2D ^{19}F—^{19}F correlation spectra of mixed fluorinated M2TM peptides at P/L 1: 30. The spectra were measured with a CORD mixing time of 500 ms at 243 K under 8641 Hz MAS. (a) 2D spectrum of the peptide in the POPC: POPG: chol membrane. (b) 2D spectrum of the peptide in the POPC: POPG membrane. (**c**) 1D cross section of the two 2D spectra at the folded 4F-Phe47 chemical shift of −71 ppm. The F-CF_3 cross peak (dashed line) intensity is much higher in the cholesterol-containing membrane than in the cholesterol-free membrane. Asterisks (*) denote spinning sidebands of the 4F-Phe47 signal.

promote cubic phases, which possess NGC's, in PE-rich membranes [62]. We previously measured ^{31}P NMR spectra of oriented DMPC/DHPC (3:1) bicelles and found that M2CD, but not M2TM (residues 22–46), induced an isotropic ^{31}P peak, indicating the formation of a high-curvature phase [65]. To investigate if clustering of M2 tetramers is correlated with membrane curvature formation, we measured the static ^{31}P spectra of the three membranes containing M2CD at P/L 1:30 (Fig. 7). Neither of the two POPC: POPG membranes showed an isotropic peak, indicating that these two membranes maintain their lamellar morphologies. In comparison, the POPE membrane exhibits a small isotropic peak at 310 K, indicating the generation of NGC at this temperature. By comparison, pure POPE liposomes manifest a uniaxial powder pattern with no isotropic peak (Fig. 7d) [71]. Therefore, the POPE membrane induces the highest degree of M2 tetramer clustering, the least depth of insertion of Phe47, and the strongest membrane curvature.

4. Discussion

4.1. M2 clustering depends on membrane environment

The ^{19}F NMR data shown here, taken together, indicate that M2 tetramers cluster on the molecular length scale in lipid membranes, and this clustering is stronger in cholesterol-containing membranes and POPE membranes than in cholesterol-free POPC: POPG membranes. At the low temperature (−30 °C) of the ^{19}F spin diffusion experiments, the peptide motion is frozen and the lipid dynamics are also largely suppressed. Thus, the different F-CF_3 cross peak intensities in the various

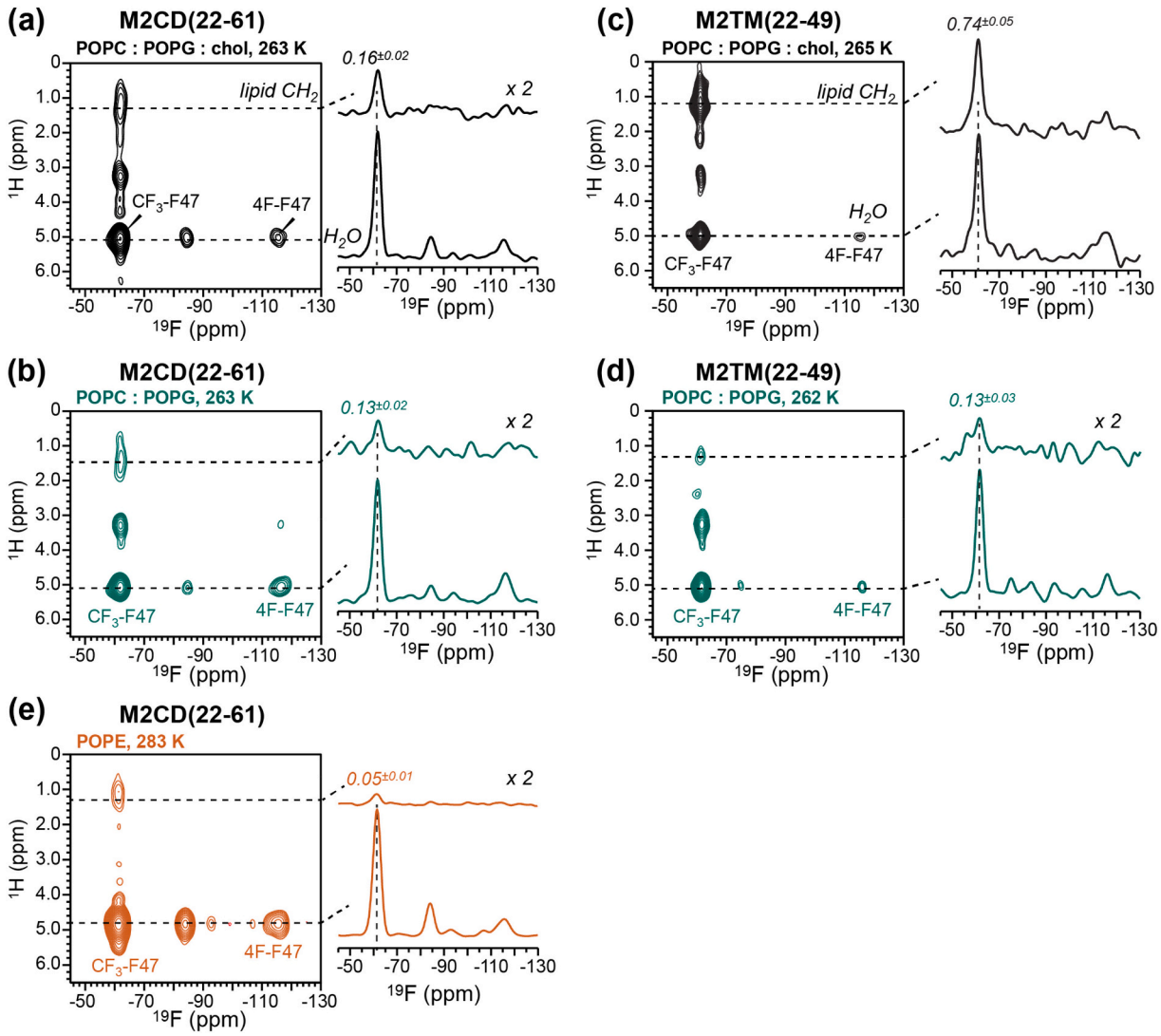

Fig. 6. 2D ^{1}H—-19F HETCOR spectra of M2 peptides in different lipid membranes. The spectra were measured at sample temperatures that give similar lipid chain ^{1}H linewidths. All samples have a P/L of 1:30. (a, b, e) M2CD spectra. (c, d) M2TM spectra. (a) Spectrum of M2CD in POPC: POPG: chol membranes measured at 263 K. (b) Spectrum of M2CD in POPC: POPG membranes measured at 263 K. (c) Spectrum of M2TM in POPC: POPG: chol membranes measured at 265 K. (d) Spectrum of M2TM in POPC: POPG membranes measured at 262 K. (e) Spectrum of M2CD in POPE membranes measured at 283 K. Water and lipid CH_2 cross sections are shown to the right of each 2D spectrum. The intensity ratio of the lipid–CF_3 cross peak relative to the water-CF_3 cross peak is the highest for M2TM in the POPC: POPG: chol membrane and the lowest for M2CD in the POPE membrane.

membranes cannot be attributed to motional differences of the peptide. By varying the peptide/lipid molar ratios and lipid compositions of the membrane, we can attribute the observed F-CF_3 cross peaks predominantly to tetramer-tetramer interactions, whereas Phe47-Phe47 contacts within a tetramer make a negligible contribution. This is because the F-CF_3 cross peaks are not present in all samples: in the cholesterol-free POPC: POPG membrane at P/L ratios of 1:30 and 1:15, the F-CF_3 cross peak of M2CD is either absent or weak, indicating that these samples exhibit neither intra-tetramer nor inter-tetramer contacts. Therefore, the Phe47-Phe47 distances within each tetramer are longer than measurable by ^{19}F spin diffusion, which is consistent with the estimated average nearest-neighbor distance of ~2.8 nm within each tetramer [52]. In contrast, clear cross peaks are observed in the POPC: POPG: cholesterol membranes, indicating that cholesterol facilitates clustering of the tetramers.

To assess whether the full AH domain is necessary for clustering, we measured 2D ^{19}F—^{19}F correlation spectra of the M2TM(22–49) peptide. The Phe47-Phe47 distances within each tetramer in this shorter peptide remain sufficiently large to prevent intra-tetramer contacts from interfering with the clustering analysis. The presence of ^{47}FFK^{49}, which resides at the TM-AH junction, should preserve the ability of this peptide to bind cholesterol [27,28]. We observed a clear F-CF_3 cross peak in POPC: POPG: chol membrane-bound M2TM(22–49), indicating that these TM peptides, in the absence of the AH, are able to form clusters in cholesterol-containing membranes.

These ^{19}F NMR data are consistent with, and more direct than, previous ^{2}H NMR spectra of the Ala_{29} CD_3 group for demonstrating clustering [25]. In that study, increasing the P/L ratio from 1:20 to 1:7.5 in the DOPC: DOPE membrane increased the uniaxial rotational correlation time of M2TM tetramers from 0.55 μs to 13.9 μs. This significant slowing of uniaxial rotation suggests clustering of the M2 tetramers. This hypothesis was further tested using coarse-grained molecular dynamics simulations, which found that M2TM tetramers cluster in an approximately linear fashion, and the tetramers can adopt both parallel and antiparallel orientations with respect to each other. Additional coarse-grained and atomistic simulations found that such M2 clusters are formed entropically at the boundaries between liquid-ordered and liquid-disordered domains of the membrane, and clustering can induce

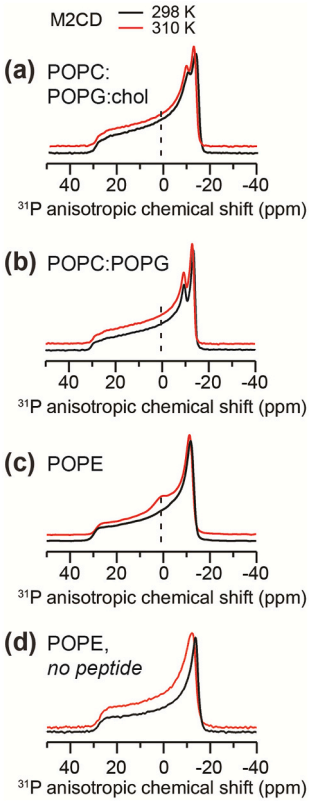

Fig. 7. Static ^{31}P NMR spectra of proteoliposomes containing M2CD at P/L 1:30. The spectra were measured at 298 K (black lines) and 310 K (red lines). (a) POPC: POPG: chol membranes. (b) POPC: POPG membranes. (c) POPE membranes. Only the M2CD-containing POPE membrane exhibits an isotropic peak, which is indicative of NGC. (d) Static ^{31}P spectra of POPE membranes without any peptide, adapted from our recent work [71]. No isotropic peak is observed, indicating that the POPE membrane maintains a lamellar morphology in the absence of M2 peptides. (For interpretation of the references to colour in this figure legend, the reader is referred to the web version of this article.)

membrane curvature [24].

EPR data of spin-labeled M2TM(residues 22–46) and M2C(residues 23–60) peptides showed an equilibrium between two conformations [51,66,67]. Both conformations are found in all membranes tested, but their relative populations change with the membrane composition. Cholesterol, thicker lipid bilayers, and PE lipids favor a "tight" conformer, which is characterized by (1) closer proximity between residues on neighboring monomers in both the TM and AH domains, (2) slower mobility of the tetramer, and (3) shallower insertion of the tetramer into the membrane and higher solvent accessibility. The first effect was demonstrated by differential spin-spin coupling between neighboring spin-labeled residues in X-band EPR spectra of M2TM [66,67] and M2TMC [51]. The second effect was demonstrated by continuous-wave EPR spectra of M2TMC [51]. Finally, the reduced membrane insertion effect was manifested using power saturation EPR experiments that probe the membrane with O_2 and the solvent with NiEDDA [51]. Interestingly, repeating these experiments with our previously used VMS membrane (SM: DPPC: DPPE: Chol) increased the population of the immobilized conformer [51]. To ensure that the two-state equilibrium reflects the properties of full-length M2, these EPR studies were extended to wild-type M2 that was nitroxide-labeled at residue 59 in the AH. Saturation recovery EPR curves exhibit a clear biexponential form that is characteristic of conformational exchange. As with other constructs, cholesterol shifted the TM and AH equilibria toward the immobile and more tightly packed conformation [68].

These EPR spectra were measured at ambient temperature (~20 °C) where cholesterol and PE can modulate the membrane viscosity and lateral pressure, which can in turn affect the tetramer conformation. However, the possibility of M2 clustering in these samples cannot be ruled out, even at the low peptide concentrations used in these studies. Even if this conformational distribution exclusively reflects intra-tetramer structural variation, it may already be reflected in the ensemble of orientational structures solved by solid-state NMR, in which the nearest-neighbor Phe47-Phe47 distances never fell below 2.1 nm [52]. These considerations together support the model that the measured ^{19}F—^{19}F cross peaks in the current 2D ^{19}F spin diffusion NMR spectra predominantly result from inter-tetramer clustering rather than intra-tetramer interactions.

4.2. Depth of insertion of M2 hinge region in lipid membranes

The fluorinated Phe47 allowed us to probe the depth of insertion of the junction between the TM and AH. While most spectra showed a modest lipid-Phe47 cross peak (Fig. 6), we observed an unexpectedly strong lipid-Phe47 cross peak for M2TM in the POPC: POPG: chol membrane. This result cannot be explained by differential dynamics of the lipids, since we measured these HETCOR spectra at temperatures that give similar lipid ^{1}H linewidths and hence similar lipid chain dynamics. Instead, we attribute this strong lipid-Phe47 cross peak to preferential interaction of the Phe47 sidechain with cholesterol, which anchors this residue to the membrane. The propensity of the Phe47 sidechain to insert into the membrane is present in M2CD as well, but may be partly restricted by the rest of the amphipathic helix. The phenylalanine residues of the AH domain of M2 have been previously reported to interact with cholesterol. In DMPC: DMPG: chol (16: 4: 5) membranes, Phe ^{13}C-labeled full-length M2 and $^{13}C_{2,3,4}$-labeled cholesterol showed cross peaks in 2D ^{13}C—^{13}C correlation spectra [29]. Further, ^{13}C—^{19}F REDOR experiments on ^{13}C-labeled protein and fluorinated cholesterol showed that an M2TM(22–46) peptide that lacks the ^{47}FFK^{49} motif does not bind cholesterol, whereas an M2CD(22–61) peptide that contains multiple Phe residues does [28]. 2D ^{13}C—^{13}C correlation spectra of ^{13}C-labeled M2(21–97) in POPC: POPG: chol membranes measured with dynamic nuclear polarization (DNP) showed cross peaks between Phe aromatic carbons and cholesterol C3 and C9 carbons [27]. Finally, docking simulations constrained by the observed intermolecular distances and cholesterol orientations found that Phe47 was the only Phe that could bind cholesterol without violating experimental constraints. These multiple lines of evidence strongly suggest that Phe47 directly interacts with cholesterol, which could explain the strong lipid-Phe47 cross peak.

We did not observe a significant difference in the depth of insertion of Phe47 in M2CD between the POPC: POPG: chol membrane and the POPC: POPG membrane (Fig. 6a, b). This result differs from power saturation EPR data of M2TMC in POPC: POPG membranes, which found that addition of 30% cholesterol caused AH residues 46, 48, 51 and 55 to be more surface exposed than they were in the non-cholesterol membrane [51]. Three experimental differences could explain this discrepancy. First, our 2D ^{1}H—^{19}F HETCOR spectra were measured in a membrane containing only 17% cholesterol. This low level of cholesterol might not cause a sufficiently large change in the AH insertion depth. Second, we conducted the HETCOR experiments at −10 °C whereas the EPR experiments were conducted at ambient temperature. Since the M2 structure is highly sensitive to the membrane properties, the low temperature at which these HETCOR spectra were measured might reduce the difference in the insertion depth of the AH. Finally, at the temperature of these 2D HETCOR experiments, the lipid chain proton linewidth of the POPC: POPG: chol membrane was ~480 Hz, which was moderately broader than the POPC: POPG lipid linewidth of ~370 Hz. Thus, the lipids may be slightly more immobilized in the cholesterol-containing membrane. If this is the case, then it is possible that the true insertion depth of Phe47 is slightly shallower in the cholesterol-containing membrane.

Interestingly, the HETCOR spectra indicate that Phe47 is less inserted in the POPE membrane than in the POPC: POPG membranes (Fig. 6e). This result is in good agreement with atomic force microscopy (AFM) data that showed that adding POPE into POPC bilayers suppressed the ability of an AH-only peptide to insert into the membrane and to modulate bilayer structure [69]. Differential insertion depth of the AH domain may allow M2 to adapt to different membrane environments, and may help modulate the interfacial energy at the L_o/L_d boundary, which is important for inducing membrane curvature [70]. Fluorescence microscopy data of M2-infected cells have shown that M2 congregates at the edge of the budding virion in the host cell membrane [19]. POPE may be recruited to budozones, as suggested by the significant POPE enrichment in influenza virions relative to the cell membranes from which they bud [59]. This POPE can promote NGC, both due to its own negative curvature and due to its ability to promote M2 clustering and regulate its depth of insertion. Thus, cholesterol, PE lipids, and M2 may jointly drive membrane scission by associating at the budozone to cause membrane curvature.

In conclusion, the current ^{19}F and ^{31}P NMR data indicate that both M2CD and M2TM tetramers form nanometer-scale clusters in lipid membranes in the presence of cholesterol and PE lipids. Based on the CF_3-F cross peaks between Phe47 residues on different peptide chains, we find the M2 tetramers to be more tightly clustered in the POPE membrane than in the 17% cholesterol POPC: POPG: chol membrane. In both membranes, the inter-tetramer distances must be shorter than 2 nm to account for the observed $^{19}F—^{19}F$ cross peaks. The membrane with the tightest M2 clusters, POPE, also exhibits the highest NGC and the shallowest insertion of the Phe47 sidechain. These results provide experimental evidence that M2 proteins cluster at the edge of the cholesterol- and PE-rich budding virion to induce membrane curvature, allowing an ever-narrowing stalk to achieve membrane scission.

Declaration of competing interest

The authors declare that they have no known competing financial interests or personal relationships that could have appeared to influence the work reported in this paper.

Acknowledgement

This work is supported by NIH grant GM088204 to M.H. This study made use of NMR spectrometers at the MIT-Harvard Center for Magnetic Resonance, which is supported by NIH grant P41 GM132079.

References

[1] Center for Disease Control and Prevention, Past Seasons Estimated Influenza Disease Burden, 2020. https://www.cdc.gov/flu/about/burden/past-seasons.html?web=1&wdLOR=c42518B89-D610-A343-B6AB-ED30749B0F5A.
[2] M. Hong, W.F. DeGrado, Structural basis for proton conduction and inhibition by the influenza M2 protein, Protein Sci. 21 (2012) 1620–1633.
[3] L.H. Pinto, L.J. Holsinger, R.A. Lamb, Influenza virus M2 protein has ion channel activity, Cell 69 (1992) 517–528.
[4] L.H. Pinto, R.A. Lamb, The M2 proton channels of influenza A and B viruses, J. Biol. Chem. 281 (2006) 8997–9000.
[5] C. Wang, R.A. Lamb, L.H. Pinto, Activation of the M2 ion channel of influenza virus: a role for the transmembrane domain histidine residue, Biophys. J. 69 (1995) 1363–1371.
[6] Y. Tang, F. Zaitseva, R.A. Lamb, L.H. Pinto, The gate of the influenza virus M2 proton channel is formed by a single tryptophan residue, J. Biol. Chem. 277 (2002) 39880–39886.
[7] L.H. Pinto, G.R. Dieckmann, C.S. Gandhi, C.G. Papworth, J. Braman, M. A. Shaughnessy, J.D. Lear, R.A. Lamb, W.F. DeGrado, A functionally defined model for the M2 proton channel of influenza A virus suggests a mechanism for its ion selectivity, Proc. Natl. Acad. Sci. U. S. A. 94 (1997) 11301–11306.
[8] F. Hu, W. Luo, M. Hong, Mechanisms of proton conduction and gating by influenza M2 proton channels from solid-state NMR, Science 330 (2010) 505–508.
[9] F. Hu, K. Schmidt-Rohr, M. Hong, NMR detection of pH-dependent histidine-water proton exchange reveals the conduction mechanism of a transmembrane proton channel, J. Am. Chem. Soc. 134 (2012) 3703–3713.
[10] J. Hu, R. Fu, K. Nishimura, L. Zhang, H.X. Zhou, D.D. Busath, V. Vijayvergiya, T. A. Cross, Histidines, heart of the hydrogen ion channel from influenza a virus: toward an understanding of conductance and proton selectivity, Proc. Natl. Acad. Sci. U. S. A. 103 (2006) 6865–6870.
[11] C. Li, M. Yi, J. Hu, H.X. Zhou, T.A. Cross, Solid-state NMR and MD simulations of the antiviral drug amantadine solubilized in DMPC bilayers, Biophys. J. 94 (2008) 1295–1302.
[12] Y. Miao, H. Qin, R. Fu, M. Sharma, T.V. Can, I. Hung, S. Luca, P.L. Gor'kov, W. W. Brey, T.A. Cross, M2 proton channel structural validation from full-length protein samples in synthetic bilayers and E. coli membranes, Angew. Chem. Int. Ed. Engl. 51 (2012) 8383–8386.
[13] S.D. Cady, K. Schmidt-Rohr, J. Wang, C.S. Soto, W.F. Degrado, M. Hong, Structure of the amantadine binding site of influenza M2 proton channels in lipid bilayers, Nature 463 (2010) 689–692.
[14] Y. Ohigashi, C. Ma, X. Jing, V. Balannick, L.H. Pinto, R.A. Lamb, An amantadine-sensitive chimeric BM2 ion channel of influenza B virus has implications for the mechanism of drug inhibition, Proc. Natl. Acad. Sci. U. S. A. 106 (2009) 18775–18779.
[15] A.L. Stouffer, R. Acharya, D. Salom, A.S. Levine, L. Di Costanzo, C.S. Soto, V. Tereshko, V. Nanda, S. Stayrook, W.F. DeGrado, Structural basis for the function and inhibition of an influenza virus proton channel, Nature 451 (2008) 596–599.
[16] S.D. Cady, T.V. Mishanina, M. Hong, Structure of amantadine-bound M2 transmembrane peptide of influenza A in lipid bilayers from magic-angle-spinning solid-state NMR: the role of Ser31 in amantadine binding, J. Mol. Biol. 385 (2009) 1127–1141.
[17] S.D. Cady, J. Wang, Y. Wu, W.F. DeGrado, M. Hong, Specific binding of adamantane drugs and direction of their polar amines in the pore of the influenza M2 transmembrane domain in lipid bilayers and dodecylphosphocholine micelles determined by NMR spectroscopy, J. Am. Chem. Soc. 133 (2011) 4274–4284.
[18] L.B. Andreas, A.B. Barnes, B. Corzilius, J.J. Chou, E.A. Miller, M. Caporini, M. Rosay, R.G. Griffin, Dynamic nuclear polarization study of inhibitor binding to the M2(18–60) proton transporter from influenza A, Biochemistry 52 (2013) 2774–2782.
[19] J.S. Rossman, X. Jing, G.P. Leser, R.A. Lamb, Influenza virus M2 protein mediates ESCRT-independent membrane scission, Cell 142 (2010) 902–913.
[20] E.A. Bruce, L. Medcalf, C.M. Crump, S.L. Noton, A.D. Stuart, H.M. Wise, D. Elton, K. Bowers, P. Digard, Budding of filamentous and non-filamentous influenza A virus occurs via a VPS4 and VPS28-independent pathway, Virology 390 (2009) 268–278.
[21] B.J. Chen, R.A. Lamb, Mechanisms for enveloped virus budding: can some viruses do without an ESCRT? Virology 372 (2008) 221–232.
[22] J. Chojnacki, T. Staudt, B. Glass, P. Bingen, J. Engelhardt, M. Anders, J. Schneider, B. Müller, S.W. Hell, H.G. Kräusslich, Maturation-dependent HIV-1 surface protein redistribution revealed by fluorescence nanoscopy, Science 338 (2012) 524–528.
[23] J. Sajman, M. Trus, D. Atlas, E. Sherman, The L-type voltage-gated calcium channel co-localizes with syntaxin 1A in nano-clusters at the plasma membrane, Sci. Rep. 7 (2017) 11350.
[24] J.J. Madsen, J.M.A. Grime, J.S. Rossman, G.A. Voth, Entropic forces drive clustering and spatial localization of influenza A M2 during viral budding, Proc. Natl. Acad. Sci. U. S. A. 115 (2018) E8595–e8603.
[25] J. Paulino, X. Pang, I. Hung, H.X. Zhou, T.A. Cross, Influenza A M2 channel clustering at high protein/lipid ratios: viral budding implications, Biophys. J. 116 (2019) 1075–1084.
[26] C. Schroeder, H. Heider, E. Möncke-Buchner, T.I. Lin, The influenza virus ion channel and maturation cofactor M2 is a cholesterol-binding protein, Eur. Biophys. J. 34 (2005) 52–66.
[27] M.R. Elkins, I.V. Sergeyev, M. Hong, Determining cholesterol binding to membrane proteins by cholesterol (13)C labeling in yeast and dynamic nuclear polarization NMR, J. Am. Chem. Soc. 140 (2018) 15437–15449.
[28] M.R. Elkins, J.K. Williams, M.D. Gelenter, P. Dai, B. Kwon, I.V. Sergeyev, B. L. Pentelute, M. Hong, Cholesterol-binding site of the influenza M2 protein in lipid bilayers from solid-state NMR, Proc. Natl. Acad. Sci. U. S. A. 114 (2017) 12946–12951.
[29] E.V. Ekanayake, R. Fu, T.A. Cross, Structural influences: cholesterol, drug, and proton binding to full-length influenza A M2 protein, Biophys. J. 110 (2016) 1391–1399.
[30] M.R. Elkins, A. Bandara, G.A. Pantelopulos, J.E. Straub, M. Hong, Direct observation of cholesterol dimers and tetramers in lipid bilayers, J. Phys. Chem. B 125 (2021) 1825–1837.
[31] J.L. Kitevski-LeBlanc, R.S. Prosser, Current applications of 19F NMR to studies of protein structure and dynamics, Prog. Nucl. Magn. Reson. Spectrosc. 62 (2012) 1–33.
[32] N.G. Sharaf, A.M. Gronenborn, 19F-modified proteins and 19F-containing ligands as tools in solution NMR studies of protein interactions, in: Z. Kelman (Ed.), Methods in Enzymology, vol. 565, Academic Press, 2015, pp. 67–95.
[33] A.A. Shcherbakov, J. Medeiros-Silva, N. Tran, M.D. Gelenter, M. Hong, From Angstroms to nanometers: measuring interatomic distances in solid-state NMR, Chem. Rev. (2022), https://doi.org/10.1021/acs.chemrev.1c00662. In press.
[34] A.A. Shcherbakov, M. Hong, Rapid measurement of long-range distances in proteins by multidimensional 13C–19F REDOR NMR under fast magic-angle spinning, J. Biomol. NMR 71 (2018) 31–43.
[35] A.A. Shcherbakov, V.S. Mandala, M. Hong, High-sensitivity detection of nanometer 1H–19F distances for protein structure determination by 1H-detected fast MAS NMR, J. Phys. Chem. B 123 (2019) 4387–4391.
[36] A.A. Shcherbakov, M. Roos, B. Kwon, M. Hong, Two-dimensional 19F–13C correlation NMR for 19F resonance assignment of fluorinated proteins, J. Biomol. NMR 74 (2020) 193–204.

[37] M. Roos, V.S. Mandala, M. Hong, Determination of long-range distances by fast magic-angle-spinning radiofrequency-driven (19)F-(19)F dipolar recoupling NMR, J. Phys. Chem. B 122 (2018) 9302–9313.
[38] M. Roos, T. Wang, A.A. Shcherbakov, M. Hong, Fast magic-angle-spinning (19)F spin exchange NMR for determining nanometer (19)F-(19)F distances in proteins and pharmaceutical compounds, J. Phys. Chem. B 122 (2018) 2900–2911.
[39] M. Lu, M. Wang, I.V. Sergeyev, C.M. Quinn, J. Struppe, M. Rosay, W. Maas, A. M. Gronenborn, T. Polenova, (19)F dynamic nuclear polarization at fast magic angle spinning for NMR of HIV-1 capsid protein assemblies, J. Am. Chem. Soc. 141 (2019) 5681–5691.
[40] M. Wang, M. Lu, M. Fritz, C. Quinn, I.J. Byeon, C.H. Byeon, J. Struppe, W. Maas, A. M. Gronenborn, T. Polenova, Fast magic angle spinning 19F NMR of HIV-1 capsid protein assemblies, Angew. Chem. Int. Ed. Engl. 57 (2018) 16375–16379.
[41] D. Huster, X. Yao, M. Hong, Membrane protein topology probed by (1)H spin diffusion from lipids using solid-state NMR spectroscopy, J. Am. Chem. Soc. 124 (2002) 874–883.
[42] M.D. Simon, P.L. Heider, A. Adamo, A.A. Vinogradov, S.K. Mong, X. Li, T. Berger, R.L. Policarpo, C. Zhang, Y. Zou, X. Liao, A.M. Spokoyny, K.F. Jensen, B. L. Pentelute, Rapid flow-based peptide synthesis, Chembiochem 15 (2014) 713–720.
[43] G. Hou, S. Yan, J. Trébosc, J.P. Amoureux, T. Polenova, Broadband homonuclear correlation spectroscopy driven by combined R2(n)(v) sequences under fast magic angle spinning for NMR structural analysis of organic and biological solids, J. Magn. Reson. 232 (2013) 18–30.
[44] A.E. Bennett, C.M. Rienstra, M. Auger, K.V. Lakshmi, R.G. Griffin, Heteronuclear decoupling in rotating solids, J. Chem. Phys. 103 (1995) 6951–6958.
[45] A. Böckmann, C. Gardiennet, R. Verel, A. Hunkeler, A. Loquet, G. Pintacuda, L. Emsley, B.H. Meier, A. Lesage, Characterization of different water pools in solid-state NMR protein samples, J. Biomol. NMR 45 (2009) 319–327.
[46] J.S. Rossman, X. Jing, G.P. Leser, V. Balannik, L.H. Pinto, R.A. Lamb, Influenza virus M2 ion channel protein is necessary for filamentous virion formation, J. Virol. 84 (2010) 5078–5088.
[47] A. Martyna, B. Bahsoun, M.D. Badham, S. Srinivasan, M.J. Howard, J.S. Rossman, Membrane remodeling by the M2 amphipathic helix drives influenza virus membrane scission, Sci. Rep. 7 (2017).
[48] A. Martyna, B. Bahsoun, J.J. Madsen, F. Jackson, M.D. Badham, G.A. Voth, J. S. Rossman, Cholesterol alters the orientation and activity of the influenza virus M2 amphipathic helix in the membrane, J. Phys. Chem. B 124 (2020) 6738–6747.
[49] P.A. Nguyen, C.S. Soto, A. Polishchuk, G.A. Caputo, C.D. Tatko, C. Ma, Y. Ohigashi, L.H. Pinto, W.F. DeGrado, K.P. Howard, pH-induced conformational change of the influenza M2 protein C-terminal domain, Biochemistry 47 (2008) 9934–9936.
[50] S. Huang, B. Green, M. Thompson, R. Chen, J. Thomaston, W.F. DeGrado, K. P. Howard, C-terminal juxtamembrane region of full-length M2 protein forms a membrane surface associated amphipathic helix, Protein Sci. 24 (2015) 426–429.
[51] S.S. Kim, M.A. Upshur, K. Saotome, I.D. Sahu, R.M. McCarrick, J.B. Feix, G. A. Lorigan, K.P. Howard, Cholesterol-dependent conformational exchange of the C-terminal domain of the influenza A M2 protein, Biochemistry 54 (2015) 7157–7167.
[52] M. Sharma, M. Yi, H. Dong, H. Qin, E. Peterson, D.D. Busath, H.X. Zhou, T.A. Cross, Insight into the mechanism of the influenza A proton channel from a structure in a lipid bilayer, Science 330 (2010) 509–512.
[53] Y. Wu, B. Canturk, H. Jo, C. Ma, E. Gianti, M.L. Klein, L.H. Pinto, R.A. Lamb, G. Fiorin, J. Wang, W.F. DeGrado, Flipping in the pore: discovery of dual inhibitors that bind in different orientations to the wild-type versus the amantadine-resistant S31N mutant of the influenza A virus M2 proton channel, J. Am. Chem. Soc. 136 (2014) 17987–17995.
[54] S. Leekumjorn, A.K. Sum, Molecular characterization of gel and liquid-crystalline structures of fully hydrated POPC and POPE bilayers, J. Phys. Chem. B 111 (2007) 6026–6033.
[55] J. Pan, F.A. Heberle, S. Tristram-Nagle, M. Szymanski, M. Koepfinger, J. Katsaras, N. Kucerka, Molecular structures of fluid phase phosphatidylglycerol bilayers as determined by small angle neutron and X-ray scattering, Biochim. Biophys. Acta 1818 (2012) 2135–2148.
[56] N. Kučerka, M.P. Nieh, J. Katsaras, Fluid phase lipid areas and bilayer thicknesses of commonly used phosphatidylcholines as a function of temperature, Biochim. Biophys. Acta 1808 (2011) 2761–2771.
[57] S.D. Cady, T. Wang, M. Hong, Membrane-dependent effects of a cytoplasmic helix on the structure and drug binding of the influenza virus M2 protein, J. Am. Chem. Soc. 133 (2011) 11572–11579.
[58] L.B. Andreas, M.T. Eddy, J.J. Chou, R.G. Griffin, Magic-angle-spinning NMR of the drug resistant S31N M2 proton transporter from influenza A, J. Am. Chem. Soc. 134 (2012) 7215–7218.
[59] P.T. Ivanova, D.S. Myers, S.B. Milne, J.L. McClaren, P.G. Thomas, H.A. Brown, Lipid composition of viral envelope of three strains of influenza virus - not all viruses are created equal, ACS Infect. Dis. 1 (2015) 399–452.
[60] J. Zhang, A. Pekosz, R.A. Lamb, Influenza virus assembly and lipid raft microdomains: a role for the cytoplasmic tails of the spike glycoproteins, J. Virol. 74 (2000) 4634–4644.
[61] L.V. Chernomordik, M.M. Kozlov, Protein-lipid interplay in fusion and fission of biological membranes, Annu. Rev. Biochem. 72 (2003) 175–207.
[62] N.W. Schmidt, A. Mishra, J. Wang, W.F. DeGrado, G.C. Wong, Influenza virus a M2 protein generates negative Gaussian membrane curvature necessary for budding and scission, J. Am. Chem. Soc. 135 (2013) 13710–13719.
[63] Y. Yang, H. Yao, M. Hong, Distinguishing bicontinuous lipid cubic phases from isotropic membrane morphologies using (31)P solid-state NMR spectroscopy, J. Phys. Chem. B 119 (2015) 4993–5001.
[64] H. Yao, M.W. Lee, A.J. Waring, G.C. Wong, M. Hong, Viral fusion protein transmembrane domain adopts beta-strand structure to facilitate membrane topological changes for virus-cell fusion, Proc. Natl. Acad. Sci. U. S. A. 112 (2015) 10926–10931.
[65] T. Wang, M. Hong, Investigation of the curvature induction and membrane localization of the influenza virus M2 protein using static and off-magic-angle spinning solid-state nuclear magnetic resonance of oriented bicelles, Biochemistry 54 (2015) 2214–2226.
[66] K.C. Duong-Ly, V. Nanda, W.F. Degrado, K.P. Howard, The conformation of the pore region of the M2 proton channel depends on lipid bilayer environment, Protein Sci. 14 (2005) 856–861.
[67] K. Saotome, K.C. Duong-Ly, K.P. Howard, Influenza A M2 protein conformation depends on choice of model membrane, Biopolymers 104 (2015) 405–411.
[68] A.L. Herneisen, I.D. Sahu, R.M. McCarrick, J.B. Feix, G.A. Lorigan, K.P. Howard, A budding-defective M2 mutant exhibits reduced membrane interaction, insensitivity to cholesterol, and perturbed interdomain coupling, Biochemistry 56 (2017) 5955–5963.
[69] J. Pan, A. Dalzini, L. Song, Cholesterol and phosphatidylethanolamine lipids exert opposite effects on membrane modulations caused by the M2 amphipathic helix, Biochim. Biophys. Acta 1861 (2019) 201–209.
[70] A.J. García-Sáez, S. Chiantia, P. Schwille, Effect of line tension on the lateral organization of lipid membranes, J. Biol. Chem. 282 (2007) 33537–33544.
[71] M. Sutherland, B. Kwon, M. Hong, Interactions of HIV gp41's membrane-proximal external region and transmembrane domain with phospholipid membranes from (31)P NMR, Biochim. Biophys. Acta Biomembr. 1863 (11) (2021).